Combination of Laser and Thermal Sintering of Thermoelectric Ca$_3$Co$_4$O$_9$ Films

Mario Wolf[1],*, Lena Rehder[1], Frank Steinbach[1], Marvin Abt[2], Richard Hinterding[1], Ludger Overmeyer[2,3], and Armin Feldhoff[1],*

Supporting Information available online

Dedicated to Prof. Dr. rer. nat. Jürgen Caro on the occasion of his 70th birthday

The manufacturing technology of thermoelectric materials is laborious and expensive often including complex and time-intensive preparation steps. In this work, a laser sintering process of the oxide-based thermoelectric material Ca$_3$Co$_4$O$_9$ is investigated. Samples based on spray-coated Ca$_3$Co$_4$O$_9$ were prepared and subsequently sintered under various laser parameters and investigated in terms of the microstructure and thermoelectric properties. Here, the combination of laser sintering and subsequent thermal sintering proved to be a promising concept for the preparation of thermoelectric films. Laser sintering can thus make a great contribution in improving the processing of thermoelectric materials, especially when films are applied that cannot be sintered under pressure.

1 Introduction

The demand for electrical energy continues to grow, featuring an increasing desire to reduce the vast amount of wasted energy, especially in form of heat. A simple and environmentally friendly method is the conversion of wasted heat into usable electricity with thermoelectric materials [1–3]. The major advantage of *energy harvesting* via thermoelectric generators (TEGs) are their reliability in direct power conversion without moving parts, thus they can operate long term without need of exchange. However, TEGs have been used only in niche applications, like space exploration or microelectronics [4, 5], because performance is too low for wide commercial application compared to the competition. Additionally, the cost and slow production of thermoelectric materials and TEGs also prevent a wide-ranging utilization of thermoelectric power conversion [6, 7].

The thermoelectric energy conversion is based on the coupling of thermal and electronic currents within the thermoelectric material. Eq. (1) shows the underlying transport equation. When a voltage U and a temperature difference ΔT are applied at a material with the cross-sectional area A and a length l, the electrical current I_{el} and the entropy current I_S are coupled via a material tensor, containing the three main thermoelectric parameters: The isothermal electrical conductivity σ, the Seebeck coefficient α and the open-circuited entropy conductivity Λ_{OC} [8, 9].

$$\begin{pmatrix} I_{el} \\ I_S \end{pmatrix} = \frac{A}{l} \begin{pmatrix} \sigma & \sigma\alpha \\ \sigma\alpha & \sigma\alpha^2 + \Lambda_{OC} \end{pmatrix} \begin{pmatrix} U \\ \Delta T \end{pmatrix} \qquad (1)$$

The performance of a thermoelectric material can then be described by the figure of merit zT, which reflects the conversion efficiency of the thermoelectric material. It is determined as the quotient of the power factor $\sigma\alpha^2$ and the entropy conductivity Λ_{OC} (Eq. (2)) [10–12].

[1]Mario Wolf, Lena Rehder, Frank Steinbach, Richard Hinterding, Prof. Dr. rer. nat. habil. Armin Feldhoff
mario.wolf@pci.uni-hannover.de,
armin.feldhoff@pci.uni-hannover.de
Leibniz University Hannover, Institute of Physical Chemistry and Electrochemistry, Callinstraße 3A, 30167 Hannover, Germany.

[2]Marvin Abt, Prof. Dr.-Ing. Ludger Overmeyer
Institute for Integrated Production Hannover, Hollerithallee 6, 30419 Hannover, Germany.

[3]Prof. Dr.-Ing. Ludger Overmeyer
Institute of Transport and Automation Technology, An der Universität 2, 30823 Garbsen, Germany.

Wiley Online Library

$$zT = \frac{\sigma\alpha^2}{\Lambda_{OC}} \qquad (2)$$

Recently, the concept of optimizing the power factor $\sigma\alpha^2$ instead of focusing on the figure of merit zT arose in the thermoelectric community [3, 13]. The power factor directly determines the achievable maximum electrical power output of a material [14], which can be equally or more important than the conversion efficiency based on the zT value. As a result, focusing on improvement of the isothermal electrical conductivity σ and the Seebeck coefficient α can be advantageous for specific desired applications.

The most common thermoelectric materials utilized so far, such as Bi_2Te_3 [15], bring major drawbacks in their toxicity and poor thermal stability, hindering an application at elevated temperatures in air. As a result, various kinds of promising materials are investigated and improved including intermetallic phases such as Zintl [16, 17] and half-Heusler phases [18, 19], oxides [20, 21] and polymers [22]. From these, oxide-based materials are the most promising for applications at high temperatures, due to their good thermal stability in air atmosphere. Within this group, calcium cobaltite ($Ca_3Co_4O_9$, CCO) proved to be the best candidate [23, 24]. CCO is characterized by a layered crystal structure, consisting of electrically conducting CoO_2 layers and poorly conducting Ca_2CoO_3 layers that cause phonon scattering [3]. As these two subsystems exhibit incommensurable lattice parameters b_1 and b_2, the structure is described in a 4-dimensional superspace group [25]. For the thermoelectric properties of CCO, the production process plays an important role [26–28]. A high energy sintering step is required to ensure a good electrical conductivity. For this, various methods like hot pressing [29, 30], conventional sintering [31], spark plasma sintering (SPS) [32], cold sintering [33, 34] and pressureless sintering methods [35] have been investigated. However, all of these established techniques are usually quite long procedures or restricted to small amounts per sintering step.

Additionally, optimization of the manufacturing technology of materials (especially films) and TEGs is also in the focus of research. Here, printing processes and additive manufacturing are promising for fast and rapid production. Rösch et al. [36] produced a printed origami TEG, consisting of poly-3,4-ethylenedioxythiophene (PEDOT) nanowires and TiS on a thin, flexible substrate. At a temperature difference of 30 K, an electrical power output of 50 $\mu W\,cm^{-2}$ was achieved. Kim et al. [4] fabricated a flexible screen-printed TEG based on Bi_2Te_3 and Sb_2Te_3 by printing respective pastes on the substrate via a screen-printing process and rolling up the thermocouples. An electrical output power of 4 $mW\,cm^{-2}$ at a temperature difference of 50 K was achieved. Glatz et al. [37] fabricated a micro-TEG for non-planar surface applications based on copper and nickel. The fabrication process consists of four photolithography steps and four electrochemical deposition steps. Here, an electrical power output of 25 $nW\,cm^{-2}$ at a temperature

difference of 32 K was achieved. The utilization of printing processes for oxide-based materials is also promising. In a previous work [38], the authors presented a fast and simple fabrication process for an oxide-based thermoelectric generators from a combination of spray coating and laser patterning. The prototype was based on CCO and Ag on a ceramic substrate, making it applicable at high temperatures. The produced prototype achieved an electrical power density of up to 1.65 $\mu W\,cm^{-2}$ at a temperature difference of 100 K and a power factor of the CCO layer of 0.06 $\mu V\,cm^{-1}K^{-2}$. The electrical conductivity was highly limited by the high porosity and poor sintering of the CCO layer. For this process, the established sintering techniques described above are insufficient for a rapid and fast production of well sintered oxide-based thermoelectric films.

In this work, laser sintering as an alternative as well as an addition to the commonly used thermal sintering processes is therefore investigated. For this, various parameters of the utilized CO_2 laser were analyzed in terms of their influence on the microstructure and resulting electrical conductivity. Selective laser sintering (SLS) has already been investigated and is an established preparation method for other kinds of materials, especially metallic and polymeric ones, but also some ceramic materials [39–41]. For laser sintering, layers of powdered materials are usually used, which are then rapidly heated and consolidated by the laser [39]. This can be done layer after layer, building up 3-dimensional bodies. The biggest advantages of this process are the fast and rapid production and the absence of any binder [39, 41]. For SLS, usually particle sizes around 40–100 μm are considered optimal, although smaller particles can result in a better surface density and overall quality, when the particles are fixed onto the substrate to avoid agglomeration due to static force [39]. For ceramic materials, Mu et al. recently presented protonic ceramic films with a thickness of up to 200 μm and a grain size between 2 and 5 μm [41, 42]. Due to the fast and rapid process of laser processes, a laser sintering of thermoelectric materials can also be highly advantageous and significantly improve the manufacturing technology for thermoelectric materials and TEGs. Especially for the preparation of thin films, a laser sintering process can be promising for rapid production and a reduction of the high manufacturing costs.

2 Experimental Section

2.1 Sample Preparation

CCO powder was purchased from CerPoTech (Tiller, Norway) and was used as a spray coating paste by dispersing 30 wt % in isopropyl alcohol with agitation and ultrasonication. The CCO is characterized by platelets with dimensions about 500 nm in a,b-direction and about 30 nm in c-direction. SEM micrographs of the powder are shown in the Supporting Information (Fig. S1). The paste was applied to

a two-layer flexible low-temperature co-fire ceramic substrate (LTCC, DuPont 951X) with an effective substrate thickness of 440 µm via spray coating (Sogolee Airbrush HP-200). The coated substrate was dried on a heating plate at 373 K after each step. A CO_2-laser (Epilog Fusion 32 M2 Dual, 75 W maximum power, spot diameter 80 µm) was then used for laser sintering of the CCO layer. Tab. 1 shows the different laser parameters. The parameters were chosen similar to a work of Mu et al. [42], who used a power between 2 and 10 W and a defocus up to 20 mm. As the decomposition of CCO starts at approximately 1200 K in air [43], the high power of the laser can obviously result in a rapid decomposition and phase separation. As a result, a significantly higher scan speed of 200 mm s^{-1} (compared to around 1 mm s^{-1} used by Mu et al. [42]) was used here. In Tab. 1, a cycle describes the number of times the laser has passed the sample. Samples A–D have been prepared 1) via laser treatment with the respective parameters and 2) via laser treatment followed by a thermal sintering step (5 h at 873 K and 1033 K for 2 h with a heating and cooling rate of 3 K min^{-1} according to our previous work [38]). For comparison, a thermally sintered reference sample of the CCO layer spray-coated onto the LTCC substrate was prepared analogously. By this, a comparison of pure thermal sintering, pure laser sintering and combination of laser sintering and thermal sintering can be achieved. Additionally, a CCO bulk sample for comparison of the electrical conductivity, Seebeck coefficient and power factor was prepared by pressing of 1 g of CCO and subsequent sintering at 1073 K for 10 h.

Table 1. Details of the laser sintering of the CCO layers. Samples A–D were prepared with the displayed laser parameters. Every sample has been additionally prepared with a subsequent thermal sintering to investigate the combination of laser and thermal sintering at 873 K for 5 h and 1033 K for 2 h. A thermally sintered reference was prepared for comparison.

| Sample	Cycles	Scanning speed [mm s^{-1}]	Power [W]	Focus distance [mm]
Reference	–	–	–	–
A	1	200	11.25	0.0
B	1	200	7.5	10.0
C	1	200	7.5	15.0
D	10	200	7.5	17.5

2.2 Characterization

The CCO layers on the LTCC substrates were characterized as-produced by X-ray diffraction (XRD, Bruker D8 Advance with Cu-K$_\alpha$ radiation) to investigate crystallinity and identify possible decomposition processes. Additionally, grazing incidence XRD patterns were measured at a fixed angle of 4° for the X-ray source and are included in the

supporting information (Fig. S2). Microstructural characterization was done via a field-emission scanning electron microscope (FE-SEM, JEOL JSM-6700F). Fractured samples were used for SEM analysis. Additionally, the films were analyzed by a field-emission transmission electron microscope (FE-TEM, JEOL JEM-2100F-UHR) equipped with an energy dispersive X-ray spectrometer (EDXS, Oxford Instruments INCA200 TEM) for elemental analysis. For TEM analyses, cross-section views were prepared by infiltrating the sample with epoxy resin followed by polishing and grinding to achieve sufficient sample thickness. Scanning TEM (STEM) micrographs and selected area diffraction (SAED) in TEM mode were both done at 200 kV. The isothermal electrical conductivity σ was measured using a home-made modified measurement cell with a horizontal tube furnace (Carbolite) and KEITHLEY 2100 Digit Multimeters in a modified van-der-Pauw setup based on the description of Indris [44]. The Seebeck coefficient α was measured as a function of the temperature with a ProboStat A setup from NorECs with an ELITE thermal system and KEITHLEY 2100 Digit Multimeters.

3 Results and Discussions

3.1 X-ray Diffraction

In Fig. 1, the normalized XRD patterns of the CCO layers are shown. Fig. 1a compares the thermally sintered reference with the pure laser sintered samples. After laser sintering, the XRD patterns still show the presence of the CCO layer, but the intensity of all reflections are significantly lower and the background becomes very noisy. Additionally, the 0020 and 0040 reflections that correspond to the a,b-dimensions of the CCO platelets strongly decreases after laser treatment. This can be explained by a strongly decreasing crystallinity due to the high power of the laser. As a result, the reflections of the substrate also become more apparent. After laser treatment, an additional reflection at approximately 41.5° can be seen, especially in samples A and D. This could be explained by the formation of $Ca_3Co_2O_6$, which can be formed by the decomposition of CCO. As this reflection is especially intense in samples A and D, the corresponding reflections of CCO are less pronounced in the normalized XRD pattern. Grazing incidence XRD patterns of the films have been also measured and are included in the Supporting Information (Fig. S2). Interestingly, the grazing incidence XRD pattern do not show the formation of $Ca_3Co_2O_6$ on the surface after laser treatment, but also show the strongly decreasing overall crystallinity and vanishing 0020 and 0030 reflections of the platelets. Additionally, only sample C shows the 1101 reflection. This could be explained by the laser parameters, as sample C was treated by the lowest power and simultaneously highest focus distance, which should result in the least impact on the film. Although the platelets were also mostly destroyed,
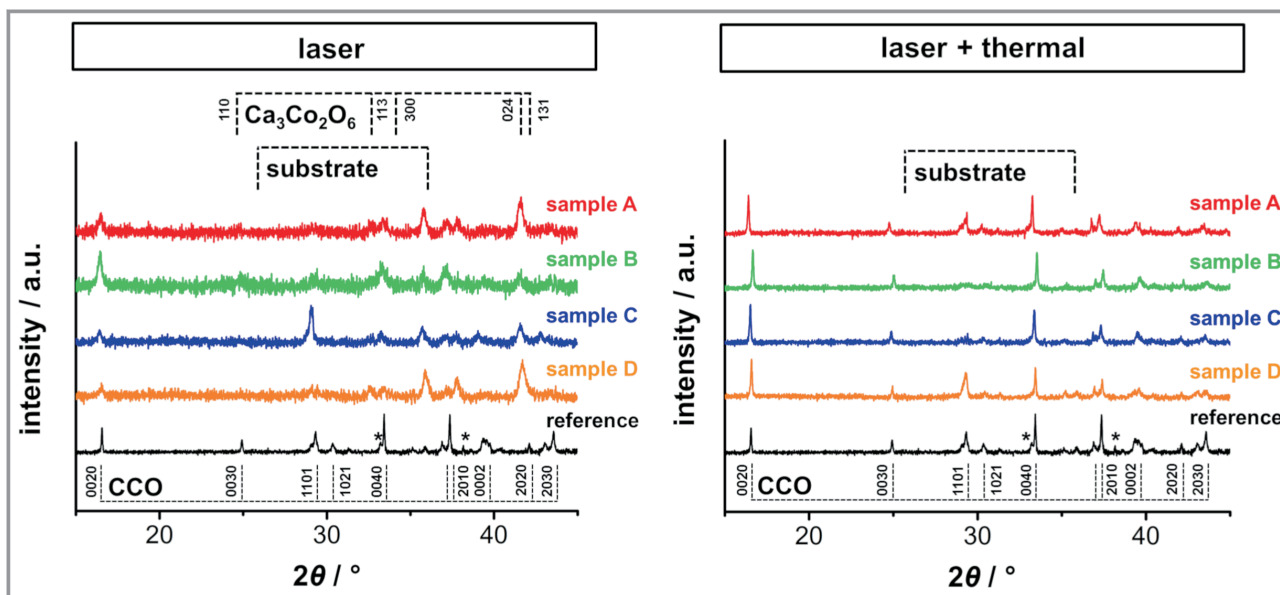
Figure 1. Normalized XRD patterns of thermally sintered reference and samples A–D after a) only laser sintering and b) the combination of laser sintering and thermal sintering. Literature reflections and indices of the $Ca_3Co_4O_9$ reference correspond to the superspace group Cm (0 1 – p 0) [25]. The reflections of the substrate have been extracted from a measurement of the pure LTCC substrate. The asterisk corresponds to minor impurities of $CaCo_2O_4$. After laser sintering, the crystallinity of the samples is reduced, but the reflections of the CCO can still be identified. After subsequent thermal sintering, the crystallinity is restored.

smaller particles could still be present and show the 1101 reflections, which does not correspond to the a,b-dimension of the platelets.
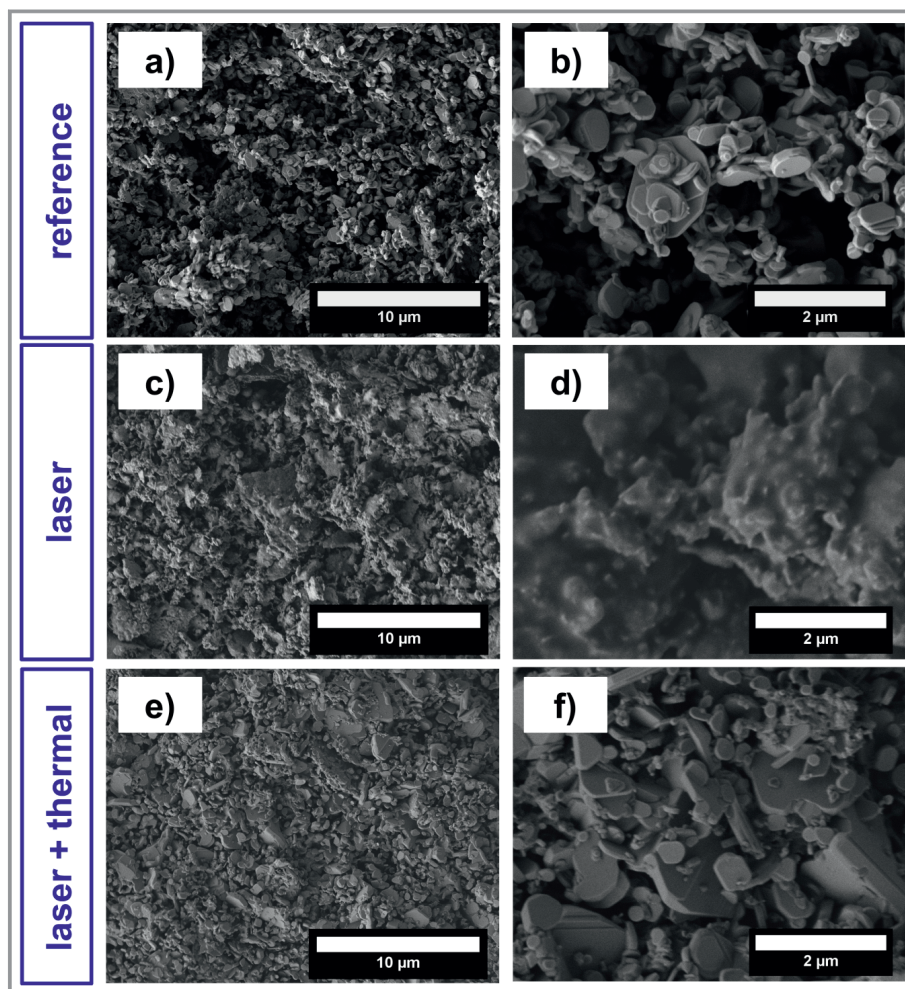
In Fig. 1b, the same comparison is shown for the combination of laser sintering and thermal sintering. Again, all XRD patterns confirm the presence of the CCO layer. The peak intensity for all samples after laser sintering and thermal sintering is relatively higher and sharper than the samples sintered only via laser treatment, which indicates that the thermal sintering restored the crystallinity of the CCO film. Additionally, the intensity of the 1101 reflection differs significantly, as it is strongly pronounced in samples A and D, while it is only implied for samples B and C. While large CCO platelets can be seen in all samples, the samples B and C show less of the smaller particles covering the platelets compared to samples A and D, which could be responsible for the intensity of the 1101 reflection.

3.2 Microstructural Analyses

SEM analysis of the thermally sintered reference sample, the laser sintered sample C and the same sample prepared via a combination of laser sintering and thermal sintering are shown in Fig. 2. The thermally sintered reference sample shows typical CCO platelets with dimension about 500 nm up to 1–2 μm in the a,b-dimension (Fig. 2a, b). The film shows a high porosity, featuring large pores with several μm in size (see Supporting Information Fig. S3). After laser treatment, the typical CCO particles cannot be identified anymore (Fig. 2c, d). Here, a network of melted particles

can be seen in the micrographs. As no defined particles can be seen here, the laser treatment could lead to a melting of the film resulting in an amorphous region on top of the film. This assumption corresponds to the strongly decreasing reflection intensity in the XRD pattern (cf. Fig. 1) and absence of the 0020 and 0030 reflections in the grazing incidence XRD pattern (Fig. S2). The other samples A, B and D show a similar behavior of a melted particle network with slight differences based on the varying laser parameters (see Supporting Information, Fig. S4). After subsequent thermal sintering, the CCO platelets can be seen again (Fig. 2e, f). Compared to the thermally sintered reference, larger platelets up to several μm in a,b-dimension and a slightly denser network could be achieved (Fig. S3–S5). The samples A, B and D again similarly show large CCO platelets after sintering (see Fig. S5).

The layer thickness of all prepared samples has been analyzed via cross-sectional SEM images, which is shown in Fig. 3. The cross-sectional SEM micrographs of sample C after laser sintering (Fig. 3a) and combination of laser and thermal sintering (Fig. 3b) show the porous CCO layer on top of the LTCC substrate. Fig. 3c shows a comparison of the layer thickness of all prepared samples according to cross-sectional SEM micrographs. The layer thickness and the error bars were determined as the median of the layer thickness at various points alongside the samples. Because the spray coating and all sintering steps are done pressureless, the samples show a strong topography and the error bars of the resulting values for the layer thickness are comparably large. After laser sintering, the layer thickness slightly decreases for all samples, as the laser treatment also

Figure 2. Top-view SEM micrographs of sample C after a,b) thermal sintering (reference), c,d) laser sintering and e,f) combination of laser sintering and thermal sintering. The micrographs prove a melting of the CCO particles after laser sintering and show a denser sintered CCO network with larger platelets after the combination of laser and thermal sintering.

agglomerations of much smaller and spherical particles compared to the typical CCO platelets underneath (Fig. 4a, b). However, the EDXS elemental mapping in still shows a mostly homogeneous distribution of Ca and Co, similar to the typical CCO, but with some red or green spots. Therefore, no complete decomposition of CCO into CaO and Co_3O_4, the typical decomposition products [43], can be found. The few green and red spots that can be identified indicate a starting phase separation of Ca and Co due to the high energy of the laser. Therefore, we assume the formation of some other Ca-Co-O phases such as $Ca_3Co_2O_6$ or $CaCo_2O_4$ [43, 45] alongside separated CaO and presumably CoO or Co_3O_4 after the laser treatment, corresponding to the finding of the XRD analyses.

After subsequent thermal sintering, the first 2–3 µm seem to be less porous compared to the area underneath and are characterized by large platelets with a homogeneous distribution of Ca and Co (Fig. 4c, d), showcasing a better sintering of the particles within the laser treated area. Selected area electron diffraction (SAED) of the top film of spherical particles (Fig. 5b) exhibit a diffuse diffraction near the main beam, indicating amorphous regions analogously to the findings of the XRD patterns. The CCO platelets underneath do not show a diffuse diffraction (Fig. 5c). These results indicate that a laser treatment before thermal sintering results in much smaller, spherical and amorphous regions that show an initial sintering process. The subsequent thermal sintering then results in a denser area with well sintered, larger CCO particles. This however only occurs in the first 2–3 µm of the film, while the rest of the film seems to be mostly unaffected. Compared to other selective laser sintering processes of ceramics [41, 42], this is a quite low impacted area, probably due to the high scanning speed of 200 mm s^{-1} and high focus distance of the laser, which, however, is required to avoid a decomposition of CCO, which presumably already started at the high scanning speed used, as indicated by the small red and green spots.
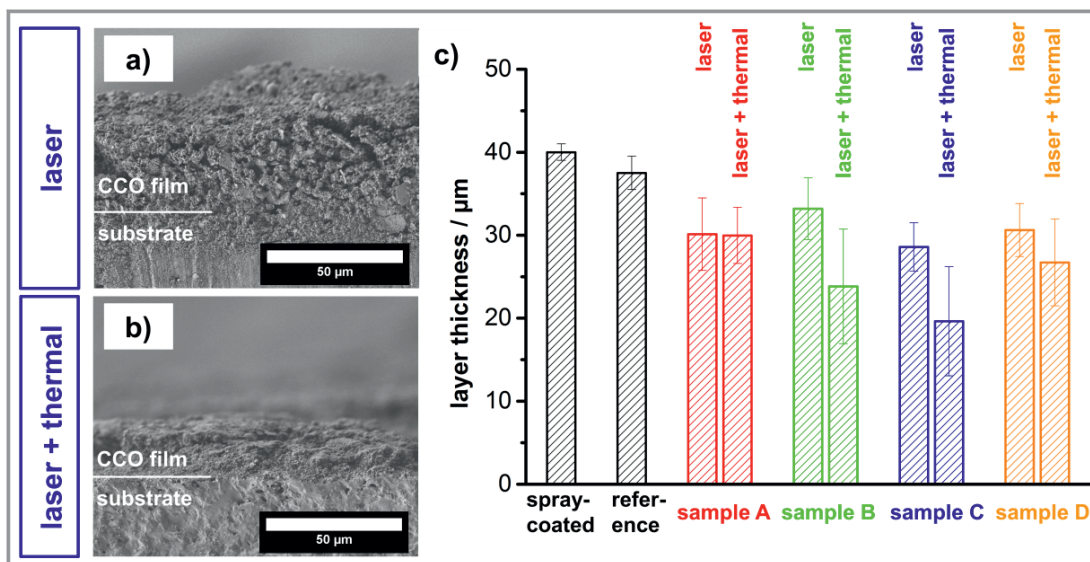
results in an ablation of particles and agglomerates. As the ablated parts may just drop onto the film again, the layer becomes even rougher, leading to an even bigger error bar. The subsequent thermal sintering leads to an additional slight shrink of all layers. For samples A and B, the shrinkage is quite low and similar to the reference sample, while in samples C and D the layer thickness shows a stronger decrease. This indicates that the subsequent thermal sintering of samples C and D leads to a denser CCO film as a result of the previous laser treatment. The cross-sectional SEM micrographs (Fig. S5) support this by showing denser layers of particle networks compared to the thermally sintered reference.

To further analyze the laser sintering process of the CCO layer, TEM analyses of the laser-sintered sample C as well as the combination of laser and thermal sintering of the same sample were done, shown in Fig. 4. After laser sintering, the top 2–3 µm of the CCO film are characterized by

Figure 3. Layer thickness analyses of the prepared samples. Cross-sectional SEM micrographs of sample C after a) laser sintering and b) combination of laser sintering and thermal sintering. c) Comparison of the layer thickness of the spray-coated CCO film, the thermally sintered reference sample and samples A–D after laser sintering and the combination of laser and thermal sintering.
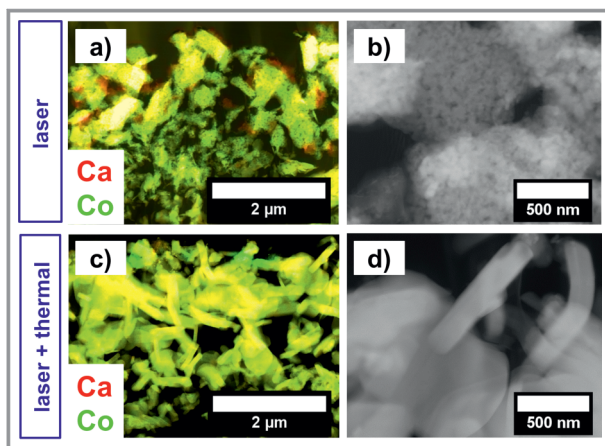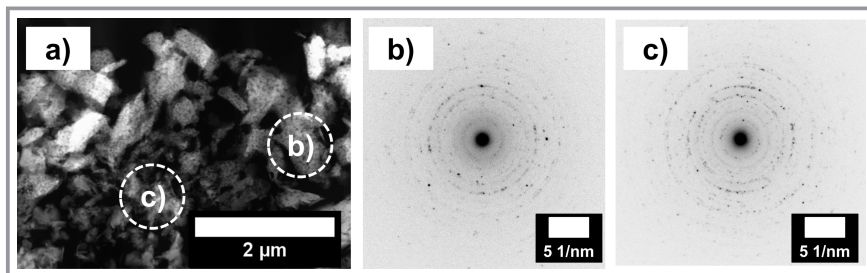

Figure 4. Cross-sectional STEM analysis of a,b) laser-sintered sample and c,d) combination of laser and thermal sintering in sample C. The EDXS elemental distributions in a) and c) show homogeneous distributions of Ca (red) and Co (green). The high-resolution STEM annular dark-field micrograph of the laser-sintered sample in b) exhibits small spherical particles in the first 2–3 µm of the CCO film, with the typical platelet particles underneath. After subsequent thermal sintering, the respective 2–3 µm can be still identified, characterized by large sintered CCO platelets, shown in d).

3.3 Thermoelectric Characterization

Fig. 6 presents the electrical conductivity of measured samples. In Fig. 6a, the comparison of an as-prepared spray-coated CCO layer, the pure laser-sintered sample C, a conventional thermally sintered reference sample and the combination of laser and thermal sintering is shown. By pure laser sintering, the electrical conductivity increases by 2 to 3 orders of magnitude compared to the pristine spray-coated CCO layer, proving the initial sintering due to the laser treatment. The electrical conductivity of a thermally sintered reference sample is around 2 to $4\,S\,cm^{-1}$ (cf. [38]). Via combination of laser and thermal sintering, the resulting electrical conductivity is again up to one order of magnitude higher. This is shown in Fig. 6b in detail. Here, sample C exhibits the highest electrical conductivity of approximately $18\,S\,cm^{-1}$ at 773 K. Samples A and B also show an increased electrical conductivity, while sample D exhibits roughly the same values as the pure thermally sintered reference sample. The higher electrical conductivity as a consequence of the combination of laser sintering and thermal sintering is in good agreement with the findings of the microstructural characterization. The resulting denser layer with well sintered particles in the top 2 to 3 µm is highly beneficial for the electrical conductivity. However, due to the remaining layer being mostly unchanged and therefore highly porous with smaller, poorly sintered platelets, the film is still characterized by a lower electrical conductivity compared to the bulk CCO sample.

In Fig. 6c, the measured Seebeck coefficient α of the thermally sintered reference, the prepared Samples A–D and a CCO bulk sample for comparison are shown. The samples B and C show a slightly increased Seebeck coefficient while samples A and D are characterized by a slightly decreased Seebeck coefficient. Consequently, samples B and C achieved a higher power factor up to $0.4\,\mu W\,cm^{-1}K^{-2}$ compared to the thermally sintered reference. The prepared CCO bulk sample still shows a higher power factor up to $1.5\,\mu W\,cm^{-1}K^{-2}$ as a result of the higher electrical conductivity and higher Seebeck coefficient. The values of the

Figure 5. SAED analyses of the laser-sintered sample C. a) Cross-sectional STEM annular dark-field micrograph with marked spots for SAED. SAED within the laser treated area b) shows diffuse diffraction near the primary beam (radius approximately 3.2 1/nm around the primary beam), supporting the hypothesis of amorphous regions due to the high power of the laser. Underneath the first 2 to 3 μm, the SAED in c) does not show this diffuse diffraction.

prepared CCO bulk sample are in the typical range compared to reported values for undoped CCO at this temperature [26, 28, 46].

3.4 Influence of Laser Parameters

Overall, the laser treatment resulted in melted and sintered networks of mostly amorphous particles (see Fig. S4). A higher laser power (sample A) and multiple cycles (sample D) both resulted in a strongly melted network and high topography of the film. A lower focus distance (sample B) also resulted in a stronger melted network, compared to a higher focus distance (sample C). After subsequent sintering, the crystallinity of all films could be restored, resulting in large CCO platelets (see Fig. S5). However, the preparation with the higher power (sample A) or with higher amount of cycles (sample D) did not result in an increase of the thermoelectric properties, while the samples prepared with 7.5 W and one cycle
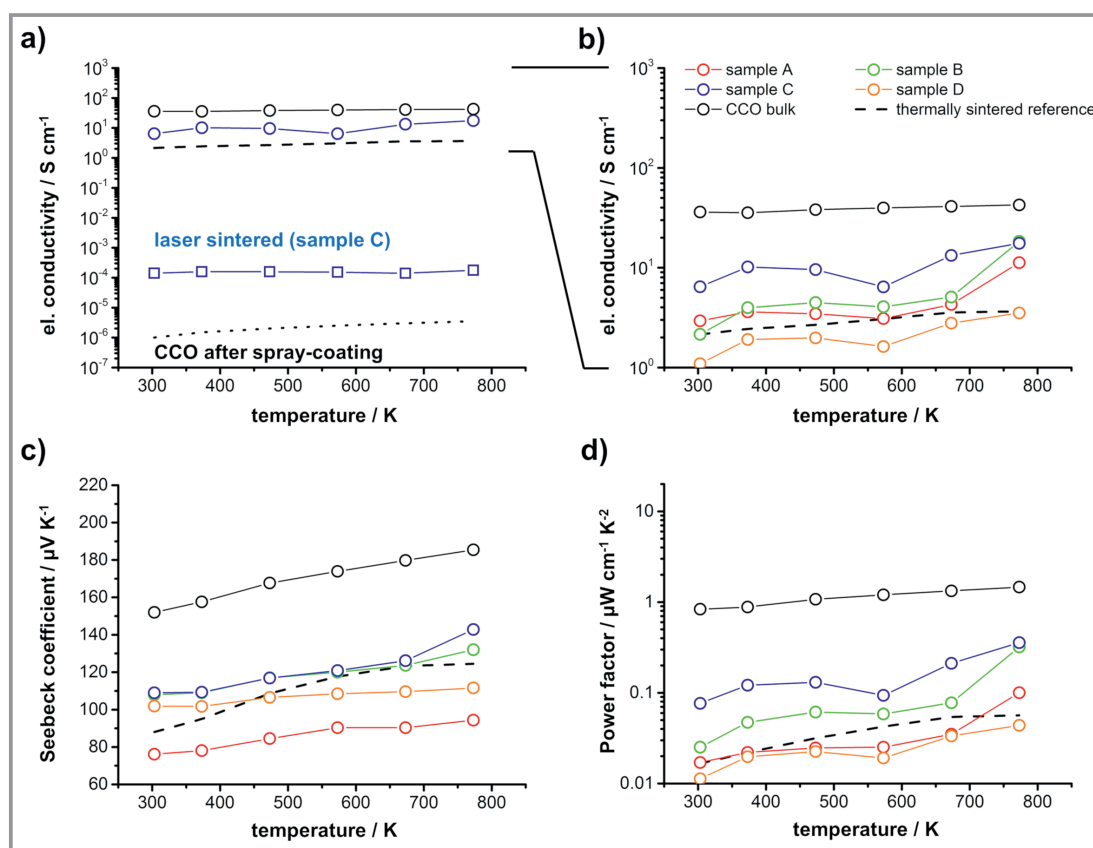
Figure 6. Temperature-dependent electrical conductivity σ, Seebeck coefficient α and calculated power factor of the prepared samples. a) Comparison of spray-coated CCO film, reference sample, laser sintering and combination of laser and thermal sintering. b) Electrical conductivity and c) Seebeck coefficient of samples A–D after combination of laser and thermal sintering and comparison to the thermally sintered reference sample. The resulting electrical conductivity and consequently the power factor of the samples B and C shown in d) is increased compared to the thermally sintered reference.

(samples B, C) both showed a noteworthy increase in the electrical conductivity, resulting in a peak power factor of $0.4\,\mu W\,cm^{-1}K^{-2}$ at 773 K, which corresponds to an increase of approximately one order of magnitude compared to the thermally sintered reference. Additionally, a higher focus distance of 15 mm (sample C) showed slightly better results compared to 10 mm focus distance (sample B). Based on the TEM microstructural analyses of sample C, via the investigated laser parameters mainly the top 2 to 3 μm of the film were influenced by the laser treatment, as a result of the high scanning speed. However, this resulted in a strongly increased electrical conductivity after subsequent thermal sintering, due to a denser layer with larger and well sintered CCO particles. This shows the potential of a laser sintering process in the manufacturing of ceramic thermoelectric films. Via further investigation and variation of the vast amount of laser parameters, the influence of the parameters can be investigated in more details and the resulting thermoelectric properties may be further enhanced.

4 Conclusions

A promising optimization for manufacturing of oxide-based thermoelectric materials is presented by laser sintering of a CCO layer. The laser sintering of a spray-coated CCO layer mostly impacted the top 2 to 3 μm of the film, resulting in much smaller, spherical, amorphous regions after laser treatment. Via a subsequent thermal sintering, the crystallinity within this 2 to 3 μm could be restored and the film was characterized by a denser layer and larger CCO platelets. As a result, the film showed a strongly increased electrical conductivity of approximately $18\,S\,cm^{-1}$, resulting in a power factor of $0.4\,\mu W\,cm^{-1}K^{-2}$ at 773 K. A stand-alone laser sintering without subsequent thermal sintering did not result in increased properties. Nevertheless, these results prove the potential of a supporting laser sintering in the manufacturing of ceramic thermoelectric films and, consequently, the manufacturing of TEGs.

Supporting Information

Supporting Information for this article can be found under DOI: https://doi.org/10.1002/cite.202100128.

References

[1] J. He, T. M. Tritt, *Science* **2017**, *357 (6358)*, eaak9997. DOI: https://doi.org/10.1126/science.aak9997

[2] A. J. Minnich, M. S. Dresselhaus, Z. F. Ren, G. Chen, *Energy Environ. Sci.* **2009**, *2 (5)*, 466–479. DOI: https://doi.org/10.1039/b822664b

[3] M. Wolf, R. Hinterding, A. Feldhoff, *Entropy* **2019**, *21*, 1058. DOI: https://doi.org/10.3390/e21111058

[4] S. J. Kim, J. H. We, B. J. Cho, *Energy Environ. Sci.* **2014**, *7 (6)*, 1959–1965. DOI: https://doi.org/10.1039/c4ee00242c

[5] L. E. Bell, *Science* **2008**, *321 (5895)*, 1457–1461. DOI: https://doi.org/10.1126/science.1158899

[6] R. He, G. Schierning, K. Nielsch, *Adv. Mater. Technol.* **2018**, *3 (4)*, 1700256. DOI: https://doi.org/10.1002/admt.201700256

[7] M. Orrill, S. LeBlanc, *J. Appl. Polym. Sci.* **2017**, *134 (3)*, 44256. DOI: https://doi.org/10.1002/app.44256

[8] A. Feldhoff, *Entropy.* **2020**, *22*, 803. DOI: https://doi.org/10.3390/e22080803

[9] H. U. Fuchs, *Energy Harvest. Syst.* **2014**, *1 (3–4)*, 1–18. DOI: https://doi.org/10.1515/ehs-2014-0011

[10] A. Feldhoff, *Energy Harvest. Syst.* **2015**, *2 (1–2)*, 517. DOI: https://doi.org/10.1515/ehs-2014-0040

[11] H. U. Fuchs, *The Dynamics of Heat – A Unified Approach to Thermodynamics and Heat Transfer*, 2nd ed., Springer-Verlag, New York **2010**.

[12] A. F. Ioffe, *Semiconductor Thermoelements, and Thermoelectric Cooling.*, 1st ed., Info-Search Ltd., London **1957**.

[13] D. Narducci, *Appl. Phys. Lett.* **2011**, *99 (10)*, 102104. DOI: https://doi.org/10.1063/1.3634018

[14] M. Bittner, N. Kanas, R. Hinterding, F. Steinbach, J. Räthel, M. Schrade, K. Wiik, M. Einarsrud, A. Feldhoff, *J. Power Sources.* **2019**, *410–411*, 143–151. DOI: https://doi.org/10.1016/j.jpowsour.2018.10.076

[15] H. Mamur, M. R. A. Bhuiyan, F. Korkmaz, M. Nil, *Renewable Sustainable Energy Rev.* **2018**, *82*, 4159–4169. DOI: https://doi.org/10.1016/j.rser.2017.10.112

[16] F. Gascoin, S. Ottensmann, D. Stark, S. M. Haïle, G. J. Snyder, *Adv. Funct. Mater.* **2005**, *15 (11)*, 1860–1864. DOI: https://doi.org/10.1002/adfm.200500043

[17] J. Shuai, J. Mao, S. Song, Q. Zhang, G. Chen, Z. Ren, *Mater. Today Phys.* **2017**, *1*, 74–95. DOI: https://doi.org/10.1016/j.mtphys.2017.06.003

[18] J. S. Poon, *Metals (Basel)* **2018**, *8 (12)*, 989. DOI: https://doi.org/10.3390/met8120989

[19] H. Zhu et al., *Nat. Commun.* **2018**, *9 (1)*, 1–9. DOI: https://doi.org/10.1038/s41467-018-04958-3

[20] J. W. Fergus, *J. Eur. Ceram. Soc.* **2012**, *32 (3)*, 525–540. DOI: https://doi.org/10.1016/j.jeurceramsoc.2011.10.007

[21] N. Kanas, S. P. Singh, M. Rotan, M. Saleemi, M. Bittner, A. Feldhoff, T. Norby, K. Wiik, T. Grande, M.-A. Einarsrud, *J. Eur. Ceram. Soc.* **2018**, *38 (4)*, 1592–1599. DOI: https://doi.org/10.1016/j.jeurceramsoc.2017.11.011

[22] L. M. Cowen, J. Atoyo, M. J. Carnie, D. Baran, B. C. Schroeder, *ECS J. Solid State Sci. Technol.* **2017**, *6 (3)*, N3080–N3088. DOI: https://doi.org/10.1149/2.0121703jss

[23] V. Rogé, F. Delorme, A. Stolz, A. Talbi, N. Semmar, J. Perrière, F. Giovannelli, E. Millon, *Mater. Chem. Phys.* **2019**, *221*, 361–366. DOI: https://doi.org/10.1016/j.matchemphys.2018.09.069

[24] F. Delorme, F. Giovannelli, *J. Electroanal. Chem. Interfacial Electrochem.* **2018**, *40*, 107–114. DOI: https://doi.org/10.1007/s10832-018-0109-2

[25] Y. M. Iyazaki, M. O. Noda, T. O. Ku, M. K. Ikuchi, Y. I. Shii, *J. Phys. Soc. Jpn.* **2002**, *71 (2)*, 491–497. DOI: https://doi.org/10.1143/JPSJ.71.491

[26] M. Bittner, L. Helmich, F. Nietschke, B. Geppert, O. Oeckler, A. Feldhoff, *J. Eur. Ceram. Soc.* **2017**, *37 (13)*, 3909–3915. DOI: https://doi.org/10.1016/j.jeurceramsoc.2017.04.059

[27] S. Bresch, B. Mieller, C. Selleng, T. Stöcker, R. Moos, T. Rabe, *J. Electroceramics.* **2018**, *40 (3)*, 225–234. DOI: https://doi.org/10.1007/s10832-018-0124-3

[28] S. Bresch, B. Mieller, D. Schoenauer-Kamin, R. Moos, F. Giovanelli, T. Rabe, *J. Appl. Phys.* **2019**, *126 (7)*, 075102. DOI: https://doi.org/10.1063/1.5107476

[29] N. Puri, R. P. Tandon, A. K. Mahapatro, *Ceram. Int.* **2018**, *44 (6)*, 6337–6342. DOI: https://doi.org/10.1016/j.ceramint.2018.01.024

[30] H. Wang, X. Sun, X. Yan, D. Huo, X. Li, J. G. Li, X. Ding, *J. Alloys Compd.* **2014**, *582*, 294–298. DOI: https://doi.org/10.1016/j.jallcom.2013.07.145

[31] K. Koumoto, R. Funahashi, E. Guilmeau, Y. Miyazaki, A. Weidenkaff, Y. Wang, C. Wan, *J. Am. Ceram. Soc.* **2013**, *96 (1)*, 1–23. DOI: https://doi.org/10.1111/jace.12076

[32] J. G. Noudem, M. Prevel, A. Veres, D. Chateigner, J. Galy, *J. Electroceramics.* **2009**, *22 (1–3)*, 91–97. DOI: https://doi.org/10.1007/s10832-008-9421-6

[33] J. Guo, R. Floyd, S. Lowum, J. P. Maria, T. Herisson De Beauvoir, J. H. Seo, C. A. Randall, *Annu. Rev. Mater. Res.* **2019**, *49*, 275–295. DOI: https://doi.org/10.1146/annurev-matsci-070218-010041

[34] A. Moraes dos Santos, D. Thomazini, M. V. Gelfuso, *Ceram. Int.* **2020**, *46 (9)*, 14064–14070. DOI: https://doi.org/10.1016/j.ceramint.2020.02.206

[35] T. Schulz, J. Töpfer, *J. Alloys Compd.* **2016**, *659*, 122–126. DOI: https://doi.org/10.1016/j.jallcom.2015.11.001

[36] A. G. Rösch, A. Gall, S. Aslan, M. Hecht, L. Franke, M. M. Mallick, L. Penth, D. Bahro, D. Friderich, U. Lemmer, *npj Flex. Electron.* **2021**, *5 (1)*, 1–8. DOI: https://doi.org/10.1038/s41528-020-00098-1

[37] W. Glatz, S. Muntwyler, C. Hierold, *Sens. Actuators, A* **2006**, *132 (1)*, 337–345. DOI: https://doi.org/10.1016/j.sna.2006.04.024

[38] M. Wolf, M. Abt, G. Hoffmann, L. Overmeyer, A. Feldhoff, *Open Ceram.* **2020**, *1*, 100002. DOI: https://doi.org/10.1016/j.oceram.2020.100002

[39] R. D. Goodridge, C. J. Tuck, R. J. M. Hague, *Prog. Mater. Sci.* **2012**, *57 (2)*, 229–267. DOI: https://doi.org/10.1016/j.pmatsci.2011.04.001

[40] M. Schmidt, M. Merklein, D. Bourell, D. Dimitrov, T. Hausotte, K. Wegener, L. Overmeyer, F. Vollertsen, G. N. Levy, *CIRP Ann.* **2017**, *66 (2)*, 561–583. DOI: https://doi.org/10.1016/j.cirp.2017.05.011

[41] S. Mu, H. Huang, A. Ishii, Z. Zhao, M. Zou, P. Kuzbary, F. Peng, K. S. Brinkman, H. Xiao, J. Tong, *J. Power Sources Adv.* **2020**, *4*, 100017. DOI: https://doi.org/10.1016/j.powera.2020.100017

[42] S. Mu et al., *Solid State Ionics* **2018**, *320*, 369–377. DOI: https://doi.org/10.1016/j.ssi.2018.03.023

[43] M. Sopicka-Lizer, P. Smaczyński, K. Kozłowska, E. Bobrowska-Grzesik, J. Plewa, H. Altenburg, *J. Eur. Ceram. Soc.* **2005**, *25 (12)*, 1997–2001. DOI: https://doi.org/10.1016/j.jeurceramsoc.2005.03.222

[44] S. Indris, *Perkolation von Grenzflächen in Nanokristallinen Keramischen Kompositen*, 1st ed., Cuvillier Verlag, Göttingen **2001**.

[45] H. Tran, T. Mehta, M. Zeller, R. H. Jarman, *Mater. Res. Bull.* **2013**, *48 (7)*, 2450–2456. DOI: https://doi.org/10.1016/j.materresbull.2013.02.060

[46] R. Hinterding, Z. Zhao, M. Wolf, M. Jakob, O. Oeckler, A. Feldhoff, *Open Ceram.* **2021**, *6*, 100103. DOI: https://doi.org/10.1016/j.oceram.2021.100103